J. Phase Equilib. Diffus. (2025) 46:279–291
https://doi.org/10.1007/s11669-025-01191-6

ORIGINAL RESEARCH ARTICLE

Modelling of the Degradation of Fe9Cr Steels in High-Temperature CO_2

Yilun Gong[1,2] · **Roger C. Reed**[2,3] · **Henrik Larsson**[4,5] · **Colin Atkinson**[6]

Submitted: 5 April 2024 / in revised form: 28 February 2025 / Accepted: 14 April 2025 / Published online: 8 May 2025

Abstract This article considers recent progress in modelling the degradation of Fe9Cr steels exposed to high-temperature CO_2. Computational modelling is used to rationalise the mechanism of the so-called breakaway oxidation, which is shown here to be associated with the carburisation of the underlying Fe9Cr substrate of finite dimensions. Oxidation kinetics, non-steady-state carburisation kinetics, and the mass transport mechanisms are covered. The theoretical and numerical/analytical challenges are discussed, with possible ways forward being suggested. Thus, we demonstrate that the software systems built on Prof. Hillert's legacy are maturing rapidly towards engineering tools which can be used to anticipate the degradation of complex multicomponent alloys in engineering situations of relevance and significant complexity.

Keywords carburisation · characterisations · CO_2 · corrosion · modelling · oxidation · steel

1 Introduction

Software tools involving computational thermodynamics and microstructural kinetics have developed in a remarkable way, built on the pioneering contributions of Prof. Mats Hillert.[1] A traditional scientific use has been the study of reactions in metals and alloys, particularly to elucidate mechanisms of transformation and to rationalise reaction pathways.[2] Due to the fundamental nature of the underlying models and the accuracy of the underlying thermodynamic and kinetic databases, hope exists that they can evolve still further so that their accuracy can be relied upon to anticipate materials degradation and thus support decisions concerning component safety. They might then be considered true engineering tools. Here, we attempt to show that this maturity is fast approaching.

As an example, this paper concerns the reaction of 9Cr (with Cr concentration of 9 wt.%) martensitic/ferritic steels in high-temperature CO_2—as this gas serves as a thermal transfer medium for various energy applications, such as the power plants being designed and constructed based upon Brayton or Allam power cycles[3] or those involving concentrated solar power (CSP).[4] Gaseous CO_2 is also relevant to the Advanced Gas-Cooled (AGR) nuclear reactors which are responsible for generating the majority of nuclear power in the United Kingdom.[5] The design of alloys against degradation in such environments is thus

---

Dedicated to the memory of Prof. Mats Hillert.

This invited article is part of a special tribute issue of the *Journal of Phase Equilibria and Diffusion* dedicated to the memory of Mats Hillert on the 100th anniversary of his birth. The issue was organized by Malin Selleby, John Ågren, and Greta Lindwall, KTH Royal Institute of Technology; Qing Chen, Thermo-Calc Software AB; Wei Xiong, University of Pittsburgh; and *JPED* Editor-in-Chief Ursula Kattner, National Institute of Standards and Technology (NIST).

✉ Yilun Gong
y.gong@mpie.de; yilun.gong@materials.ox.ac.uk

[1] Max Planck Institute for Iron Research, Düsseldorf, Germany

[2] Department of Materials, University of Oxford, Oxford, UK

[3] Department of Engineering Science, University of Oxford, Oxford, UK

[4] Material Science Department, KTH-Royal Institute of Technology, Stockholm, Sweden

[5] Thermo-Calc Software AB, Solna, Sweden

[6] Department of Mathematics, Imperial College, London, UK

technologically important.[6] The 9Cr martensitic/ferritic steels possess good creep strength and adequate corrosion resistance in the CO_2 environment at medium temperatures between 400 to 700 °C.[7] The main character of associated phase transformations during the degradation of 9Cr martensitic/ferritic steels in these situations is simultaneous oxidation and carburisation.[8] On the one hand, the outward growth of the magnetite scale is accompanied by the inward growth of the Cr-rich Fe spinel layer. At the same time, the alloy substrate—which is beneath the thickening duplex oxide scales—is progressively carburised with the extensive formation of carbides. Those carbide phases are then oxidised,[8] consistent with conventional theory for the internal precipitation within an alloy attacked by different oxidants (Meijering,[9] as reviewed in[8]), which states that the less stable precipitate (which is carbide in this case) is expected to be found in the deeper zone.

Extensive experimental and theoretical studies have been conducted to understand and describe the phase transformations that occur in 9Cr steels when exposed to the CO_2 environment.[5,10–16] In this paper, those efforts will be considered coherently, particularly with a view to rationalising the corrosive attack which leads to so-called breakaway oxidation. The limitations of the modelling approaches taken thus far and possible ways forward will also be discussed. As will be seen, the computational approaches laid down by Prof. Mats Hillert[1,17–19] are instrumental in what has been accomplished—and what is needed moving forward.

2 Modelling Approaches

When 9Cr steel is exposed to high-temperature CO_2, various phase transformations can occur, as schematically summarised in Fig. 1. The simultaneous oxidation and carburisation reactions, as observed by experiments,[5] can be rationalised by the illustrative diffusion paths on the phase diagram as shown in Fig. 2 where the stability region of each phase is represented at different partial pressures of oxygen ($\boldsymbol{P_{O_2}}$) and carbon activities ($\boldsymbol{a_C}$).

To give quantitative predictions of those reactions, in this section (Modelling Approaches), the underlying kinetic models will be introduced, emphasising:

- Boundary conditions applied at the spinel/substrate interface due to the Boudouard reaction (section 2.1)
- Treatment of carbon diffusion and carbide precipitation in the substrate (section 2.2)
- Treatment of the oxidation kinetics (section 2.3)
- Coupling between oxidation and carburisation (section 2.4)
- Treatment of finite-size samples for engineering applications (section 2.5)

2.1 Interface Reaction at Oxide/Alloy Interface

One major characteristic of the degradation in the alloy substrate is the **non-steady-state** carburisation at low temperatures, particularly below 600 °C. This is supported by experimental measurements that the carbon concentration (or carbide fraction) in the alloy close to the scale/alloy interface increases with time (see Fig. 3(a)), and such delay in reaching local equilibrium at the interface is more profound at lower temperatures (see Fig. 3(b)).[5,10,12,20,21]

Theoretically, such phenomena can be rationalised by considering the following reactions[22]:

$$CO_2 = CO + \tfrac{1}{2} O_2 \qquad \text{(Eq 1)}$$

$$2CO = CO_2 + \underline{C} \qquad \text{(Eq 2)}$$

where a low oxygen activity, which is controlled by the oxide/alloy equilibrium, corresponds to a high P_{CO}/P_{CO_2} ratio (where P is the partial pressure) by the reaction (1), thereby producing a high carbon activity via the Boudouard reaction (reaction (2), where underlining denotes a solute species). Three possible thermally activated processes are involved:

(a) Diffusion of CO and CO_2 species across the oxide scale.
(b) Kinetics of the Boudouard reaction.
(c) Kinetics of carbon transport across the oxide/alloy interface.

Coupled processes (a) and (b) were explicitly considered in Rouillard's early work[20] which succeeded in explaining the increase with time in the rate of carbon uptake relative to that of oxygen but did not justify increased P_{CO}/P_{CO_2} at the oxide/alloy interface with time (which should be a constant concerning parabolic oxidation kinetics). Later, coupled processes (b) and (c) were proposed by Young,[8] which gives the instantaneous carbon activity of the alloy at the oxide/alloy interface $a_C^\star$ as

$$a_C^\star = a_C^{eq}[1 - \exp(-\beta t)] \qquad \text{(Eq 3)}$$

where a_C^{eq} is the equilibrium carbon activity as derived from the reaction (2) and β is a lumped kinetic parameter considering the kinetics of the Boudouard reaction and the cross-interface diffusion kinetics. Acknowledging that the sluggish Boudouard reaction is catalysed either by the metal[23] at the oxide/scale interface and/or possibly by the whole oxide scale, process (c) alone defines the carbon ingress rate across the scale/alloy interface $\boldsymbol{J_C^\star} V_m$. By applying the absolute reaction rate theory[24] and assuming

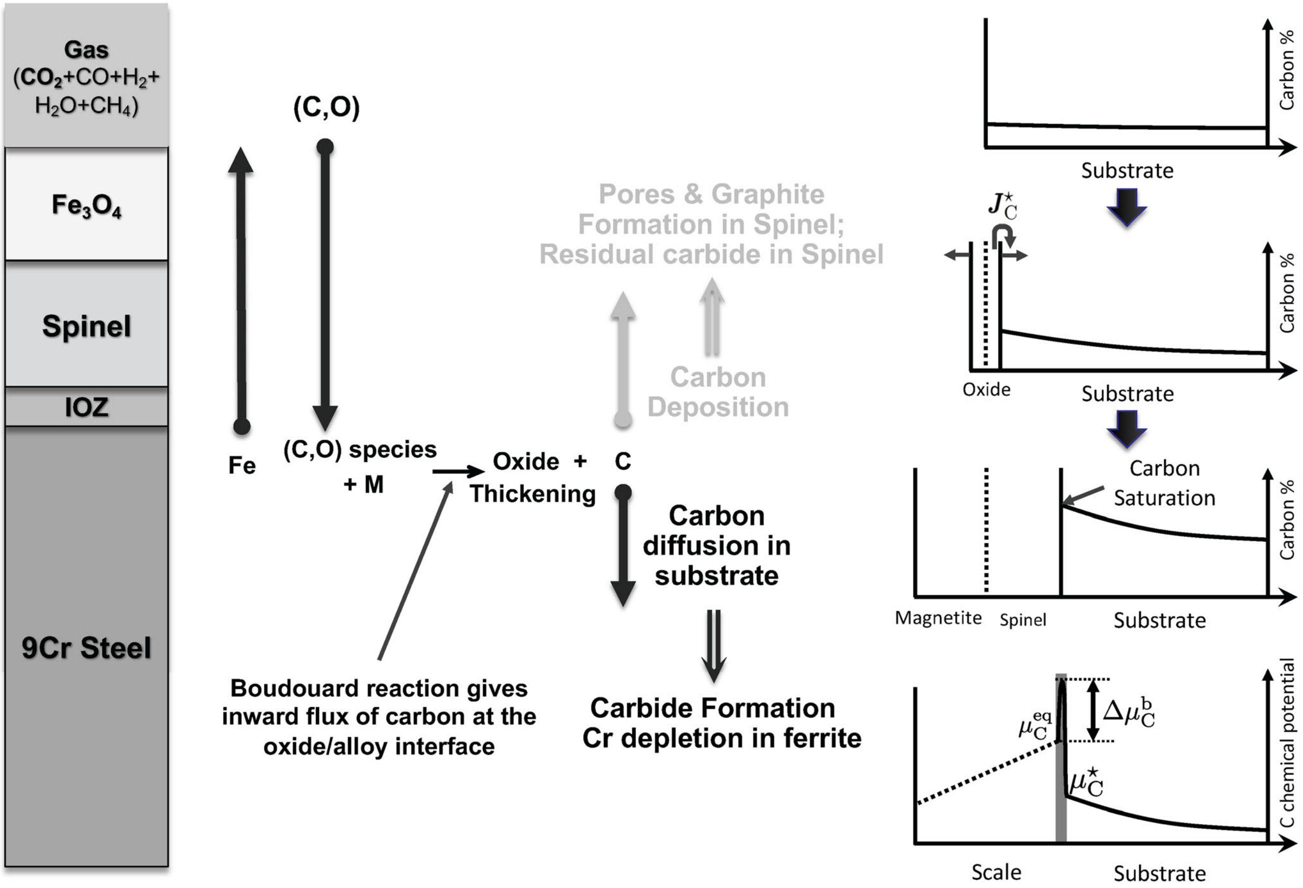

Fig. 1 Illustration of phase transformations in 9Cr steel due to high-temperature degradation in CO_2. The figure is adapted from [10]

Fig. 2 Results of thermodynamic calculations predicting phase stable regions at different P_{O_2}(relative to the gas phase at 1 bar) and a_C (relative to the graphite phase) for the Fe−9 wt.% Cr alloy at 600 °C; calculations were based on major phases included in the TCFE11 thermodynamic database; suggested (illustrative) diffusion paths for shorter times ($t_1 \neq 0$) and longer times ($t_2 > t_1$) are marked as dashed lines

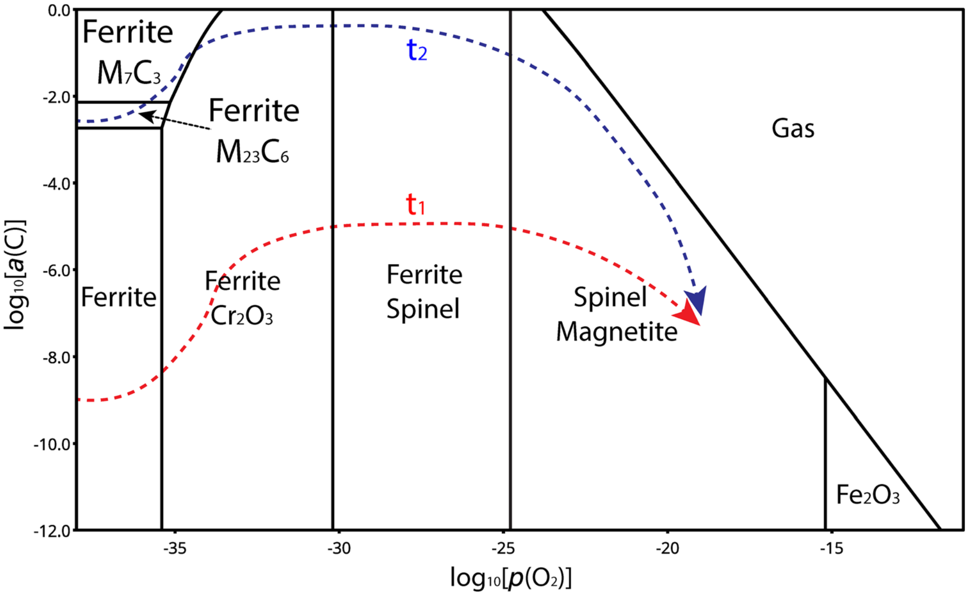

that there is an energy barrier associated with the cross-interface diffusion,[12] $J^\star_C V_m$ (where $J^\star_C$ is the flux of carbon [mol·m^{-2}·s^{-1}] and V_m is the molar volume of the alloy at the interface [m^3·mol^{-1}]) can be approximated by

$$J^\star_C V_m = \alpha_a\{T\}\left(a_C^{eq} - a_C^\star\right) \qquad \text{(Eq 4)}$$

where the Arrhenius behaviour of the kinetic constant α_a was confirmed by further experimental quantifications

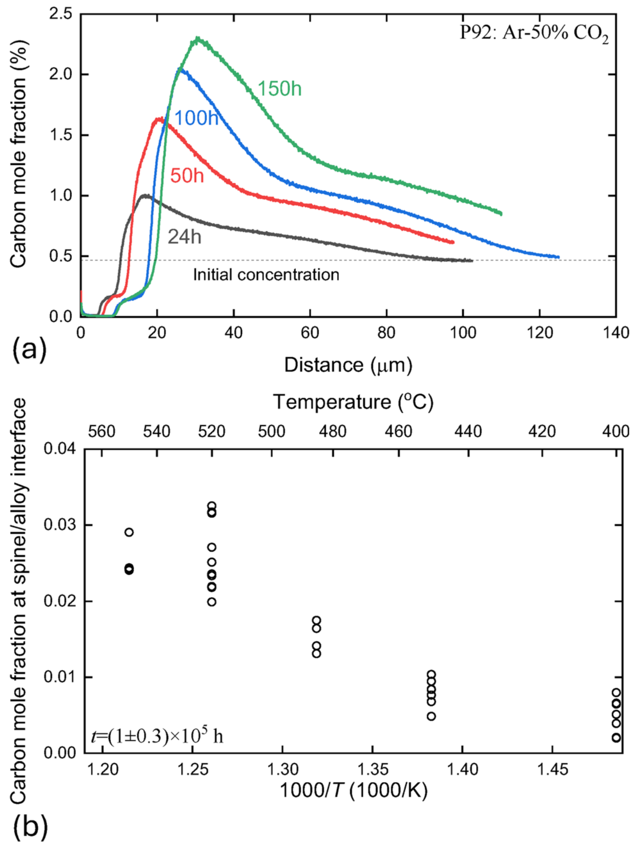

Fig. 3 (a) In-depth carbon mole fraction profile in a P92 steel (9wt.% of Cr, 2wt.% of W and 0.09wt.% of C; for more detailed composition, see [21]) reacted with Ar–50 vol.% CO$_2$ at 550 °C, measured by Glow Discharge Optical Emission Spectroscopy (GDOES), after [21]; (b) mole fraction of carbon measured at the spinel/substrate interface in a class of 9Cr steels (8.92-9.44wt.% of Cr and 0.093-0.11wt.% of C; for more detailed composition, see [10]) exposed to a CO$_2$-rich gaseous environment at different temperatures, at ~ 10^5 h, after [10]. *Reproduced by permission of Elsevier*

which give the activation energy of α_a to be about 230 kJ/mol for P91 steels (9 wt.% of Cr and 1 wt.% of Mo; for more detailed composition, see[10]) at temperatures ranging from 485 to 640 °C.[10]

2.2 Diffusion of Carbon in the Substrate

2.2.1 Homogenisation Model

The general treatment of multi-phase diffusion (and associated phase transformations) in 1D has been rationalised by the homogenisation model[25,26] (Fig. 4) which is implemented in the DICTRA software package by using the finite volume method (FVM).

In the homogenisation model, the diffusive flux of element k in a single phase in the lattice-fixed frame of reference, J_k, is given by:

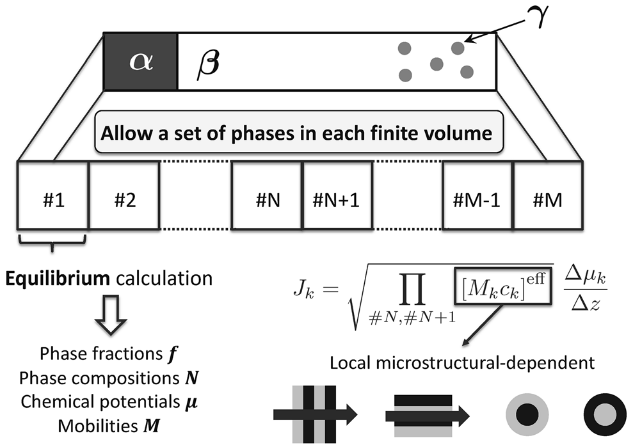

Fig. 4 Schematic illustration of the homogenisation model

$$J_k = -M_k c_k \frac{\partial \mu_k}{\partial z} \quad \text{(Eq 5)}$$

where M_k, c_k and μ_k are the mobility, concentration, and chemical potential of component k, respectively. To account for the multi-phase diffusion, J_k is given by:

$$J_k = -\Gamma_k \frac{\partial \mu_k}{\partial z} \quad \text{(Eq 6)}$$

where the homogenisation function Γ_k for element k is a function of

$$\Gamma_k^r = M_k^r c_k^r \quad \text{(Eq 7)}$$

which is evaluated for each phase r and is local phase geometry dependent. For example, the Wiener bound[27] (rule-of-mixture) defines Γ_k as a function of the volume fraction of phase r, f^r:

$$\Gamma_k = \sum\nolimits_r f^r \Gamma_k^r \quad \text{(Eq 8)}$$

It should be emphasised that both Γ_k and μ_k in Eq 6 are evaluated by assuming that at each point along the reaction front, the local phase assemblage comes to local equilibrium.

2.2.2 Application to 9Cr Steels Exposed to CO$_2$

Because the Cr concentration in the spinel phase region is close to that in the alloy, and the diffusion of substitutional elements such as chromium in the ferrite is much slower compared with that of interstitial carbon, no (long-range) chemical inhomogeneity is observed in the substrate apart from carbon. The slow diffusion of oxygen within the substrate, characterised by the shallow internal oxide zone (IOZ) beneath the spinel phase region, has limited influence on carbon ingress. The diffusion in the alloy substrate can, therefore, be simplified by considering only the carbon concentration (C_{C}) field, which can be described by the diffusion equation in a volume-fixed frame of reference as

$$\dot{C}_{\mathrm{C}} = \nabla \cdot \left(D_{\mathrm{C}}^{\mathrm{eff}} \nabla C_{\mathrm{C}}\right) \qquad \text{(Eq 9)}$$

where the effective chemical diffusion coefficient of carbon $D_{\mathrm{C}}^{\mathrm{eff}}$ can be expressed as

$$D_{\mathrm{C}}^{\mathrm{eff}} = f_{v}^{\alpha} D_{\mathrm{C}}^{\alpha} \frac{\mathrm{d}C_{\mathrm{C}}^{\alpha}}{\mathrm{d}C_{\mathrm{C}}} \qquad \text{(Eq 10)}$$

which explicitly considers carbide precipitations in the ferrite; this is important since carbon diffuses predominantly through ferrite but is mainly tied up in the carbide precipitates. Because of the slow-growing features of carbide, it is reasonable to assume a local equilibrium between carbide and ferrite (within a finite volume). Therefore, in Eq 10, the volume fraction of ferrite (f_{v}^{α}), the chemical diffusion coefficient of carbon in ferrite (D_{C}^{α}) and the carbon concentration within the ferrite (C_{C}^{α}) can all be evaluated by coupling with typical thermodynamic and (diffusional) mobility databases.[10]

Differences of $D_{\mathrm{C}}^{\mathrm{eff}}$ have been found between those calculated from Eq 10 (which is coupled with Thermo-Calc TCFE8 and MOBFE4 databases) and those derived from carbon uptake measurements, particularly at low temperatures,[10,12] possibly due to precipitation-induced strain in the ferrite.[12,13] A phenomenological correction factor, ζ, which is imposed to $D_{\mathrm{C}}^{\mathrm{eff}}$ as

$$D_{\mathrm{C}}^{\mathrm{eff,corr}} = \zeta\{C_{\mathrm{C}}, T, t\} D_{\mathrm{C}}^{\mathrm{eff}} \qquad \text{(Eq 11)}$$

was found highly C_{C},[12] time (t),[12] and temperature (T)[10] dependent.

Nevertheless, solving Eqs 9 and 10 allows for fast evaluation of the carbon diffusion field under any boundary conditions applied, such as those described in section 2.1. This is particularly useful for engineering applications where:

- Proposed physical models need to be calibrated against a large number of experimental measurements.[10]
- Sampling-based lifetime assessment requires an efficient probing of the physical status for any physical parameters assumed.[28]

2.3 Oxidation Models

Compared with relatively more extensive and more mature modelling efforts describing diffusion and associated phase transformation in alloy substrates,[1,29–31] fewer physics-based modelling approaches concentrate on the mass transport within the oxide for predictions of the thickening kinetics of the scale when exposed to high-temperature corrosive environments. One practical solution appealing to both the Wagner theory[32,33] and measured kinetics, as done in[5] for 9Cr steels, is to fit Wagner's kinetic model to measured oxidation kinetics by considering the effective diffusional mobility of ionic species as adjustable parameters; physics, such as treating how SiO_2 blocks the diffusion and enhances the oxidation resistance can therefore be rationalised in this approach. Since no defect chemistry has been explicitly considered, such approaches lack predictive capabilities when extending to arbitrary alloy compositions. There are several approaches based on the Wagner theory that emphasise the role played by the defect chemistry—these have been able to rationalise the experimentally observed parabolic kinetics and microstructural features such as void formation in thick oxide layers.[34,35]

Here, we show the general approach proposed within the CALPHAD framework for the Fe-O system[34] which is implemented in the homogenisation model as described in section 2.2.1. The thermodynamic description of defect chemistry for the solid Fe-O system was primarily assessed by Sundman.[36] It was further modified by introducing vacancies (Va) in the oxygen sublattice to account for P_{O_2} dependent oxygen mobilities.[11,34,37,38] All descriptions were formulated using the compound energy formalism (CEF)[18]:

$$\text{Wüstite}: \left(\mathrm{Fe}^{+2}, \mathrm{Fe}^{+3}, \mathrm{Va}\right)_1 \left(\mathrm{O}^{-2}, \mathrm{Va}\right)_1$$

$$\text{Magnetite}: \left(\mathrm{Fe}^{+2}, \mathrm{Fe}^{+3}\right)_1 \left(\mathrm{Fe}^{+2}, \mathrm{Fe}^{+3}, \mathrm{Va}\right)_2 \left(\mathrm{Fe}^{+2}, \mathrm{Va}\right)_2 \left(\mathrm{O}^{-2}, \mathrm{Va}\right)_4$$

$$\text{Hematite}: \left(\mathrm{Fe}^{+2}, \mathrm{Fe}^{+3}\right)_2 \left(\mathrm{Fe}^{+3}, \mathrm{Va}\right)_1 \left(\mathrm{O}^{-2}\right)_3$$

Since the ionic diffusion in oxide is highly dependent on the defect concentration, it is critical to couple with the above assessment when predicting the diffusion coefficient. A general diffusion model for mass transport in oxide was introduced by.[34,39,40] The main difference compared to those treating diffusion in metallic systems[25,26] is that the mobility M_j^r of element j in phase r has a contribution from different types of charged species in different sublattices which are independently defined, consistent with:

$$M_j^r = \frac{\sum_s a_s^r \sum_k b_{jk} y_k^{rs} z_{\mathrm{Va}}^{rs} M_{k\mathrm{Va}}^{rs}}{\sum_s a_s^r \sum_k b_{jk} y_k^{rs}} \qquad \text{(Eq 12)}$$

where $M_{k\mathrm{Va}}^{rs}$ is the mobility of species k on sublattice s in phase r, a_s^r is the number of sites on sublattice s in phase r, b_{jk} is the number of moles of element j per mole formula unit of species k and y_k^{rs} is the site fraction of species k on sublattice s in phase r. The parameter z_{Va}^{rs} is identical with y_{va}^{rs} if the vacancy is a defined constituent on the sublattice, otherwise, it is set equal to one. Equation 12 gives a rather general and complete description of ionic transport in the oxide lattice. Besides, explicit treatments of diffusive flux (and its divergence) in anion sublattice in oxides (i.e. O^{2-} as the volume carrier) allow for the evaluation of the upper bound of the amount of Kirkendall porosity.[34]

It has to be emphasised that the defect-chemistry-based oxidation model described in this section is for a rather idealised situation, such as oxidation of pure Fe, where solid-state diffusion is dominated. For CO_2 oxidation of 9Cr steels, as discussed in section 3.2, the complex microstructure of the scale may alter the mass transport mechanisms locally.

2.4 Coupling of Oxidation with Carburisation

The (semi-)coupling of oxidation and carburisation has been proposed in[10] where the flux boundary condition Eq 4 is modified by introducing a carbon partitioning term when imposed to a moving scale/alloy interface:

$$\mathbf{J}_{\mathrm{C}}^{\star} V_m = \alpha_a\{T\}\left(a_{\mathrm{C}}^{\mathrm{eq}} - a_{\mathrm{C}}^{\star}\right) + P_{\mathrm{C}} C_{\mathrm{C}}^{\star} V_m \mathbf{v}^{\star}\{t\} \qquad \text{(Eq 13)}$$

where $\mathbf{v}^{\star}$ is the time-dependent moving velocity of the spinel/alloy interface (due to oxidation), and P_{C} defines the partitioning of carbon between the scale and the alloy substrate (i.e. $P_{\mathrm{C}} = 0$ means that the spinel retains all the carbon as it grows while $P_{\mathrm{C}} = 1$ means all carbon is piled-up in the substrate ahead of the spinel). If assuming P_{C} to be time-independent, the flux of carbon deposited on the spinel phase region, $(1 - P_{\mathrm{C}}) C_{\mathrm{C}}^{\star} V_m \mathbf{v}^{\star}\{t\}$, is increasing with time as the interface migrates inwards.

This approach assumes that the carbon concentration field does not influence the oxygen concentration/chemical potential field thus the scale thickening kinetics. A reaction-based approach (which violates local-equilibrium assumptions) might be required for full coupling of oxidation and carburisation in this case, but this remains the subject of future work.

2.5 Treatment of Finite-Size Samples

Building on the models described in previous sections, it is also practically important to treat various geometries of samples, as the carbon saturation within the substrate has been found to be strongly correlated with the initiation of the breakaway oxidation.[10] The homogenisation model, which is implemented in 1D, has succeeded in rationalising the measured carbon profiles for a finite domain.[5] The efficient numerical model proposed (described in section 2.2.2) shows good agreement with the homogenisation model.[10] By extending the proposed numerical model to arbitrary 2D/3D geometries, it is possible to rationalise the carbon uptake kinetics at the component scale. As illustrated in Fig. 5, for complex 2D/3D geometries, the carbon concentration at the oxide/alloy interface also shows inhomogeneity—the corner or edge region is more susceptible to carbon saturation.

3 Discussion and Outlook

3.1 On the Challenge and Future Developments of Oxidation Models

In the oxidation model described in section 2.3 and outlined in,[34] the diffusion field is solved by using the homogenisation model, which is fully coupled with the thermodynamic description of the Fe-O system (see section 2.3), the molar volume assessment and the mobility assessment (Eq 12,[41]). This allows for predicting the evolution of (1) phase fractions and (2) the upper bound of Kirkendall porosities.

Performing such simulations, however, remains numerically challenging mainly due to:

(1) The high nonlinearity when solving the diffusion equation. The diffusive mobility of charged species, which is sensitive to the vacancy concentrations (Eq 12) and thus the magnitude of P_{O_2}, is very different across the oxide scale.

(2) The computationally demanding free energy minimisation procedure which finds the minimum free energy and associated partitioning of different charged species across different sub-lattices. In other words, the many internal degrees of freedom typically employed for oxide phases make the equilibrium calculation both numerically challenging and computationally costly.

The difficulties outlined above are even more significant for higher-order systems such as Fe-Cr-O[42] and Ni-Cr-O.[11] A possible way forward would be to parameterise the Gibbs free energy (respective to composition) for oxide phases, *i.e.* remove the internal degrees of freedom by introducing some auxiliary, preferably smooth function. Although such an approach would certainly come about at the cost of reduced accuracy, it should be a viable solution. Another numerical approach, called the 'interpolation scheme', as implemented in the DICTRA software package, is to store calculated thermodynamic equilibria in a discretised thermodynamic condition mesh, so any further equilibrium calculation that falls within the calculated conditions will be obtained by interpolating results from those at neighbouring conditions.[43] This can significantly speed up the diffusion calculations which require intensive thermodynamic equilibrium calculations. However, only the C^0 continuity has currently been implemented in the 'interpolation scheme',[34,43] i.e. the derivatives of stored

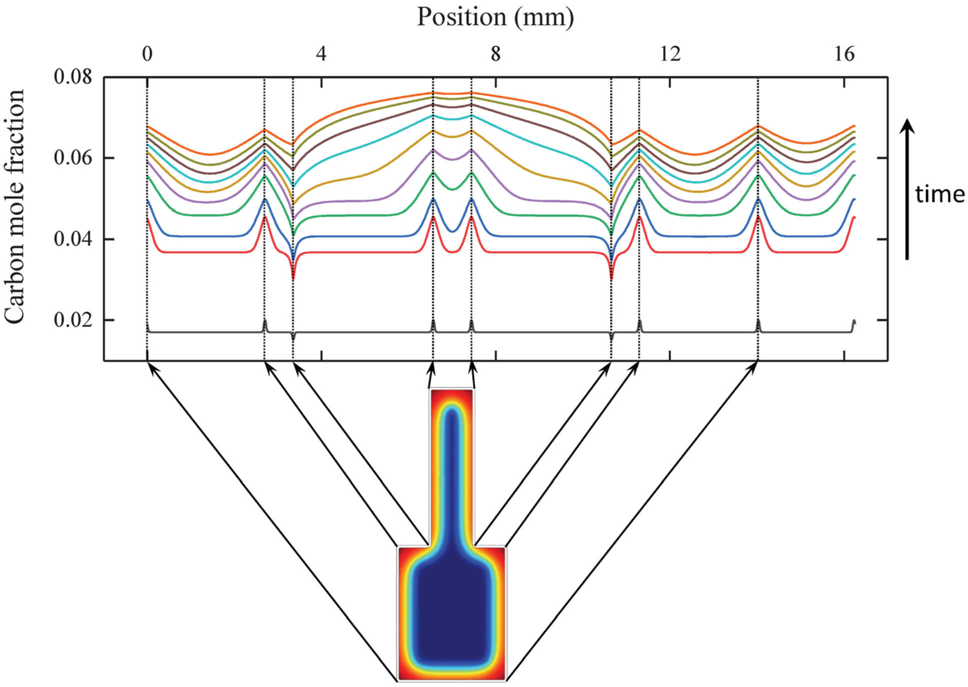

Fig. 5 Typical distributions of carbon uptake predicted at the spinel/substrate interface across a 2D domain at different times

thermodynamic equilibria with respect to the composition mesh are discontinuous. A higher degree of smoothness, i.e. a C^k continuity with $k > 0$, may allow for a coarser mesh thus much higher numerical efficiency and accuracy.

Rather than explicitly solving the time-dependent diffusion field as described above, another way to simplify the calculations, as implemented in,[44] is to transform the governing equations to a set of ordinary differential equations (ODEs) by defining

$$\xi = z/\sqrt{t} \qquad \text{(Eq 14)}$$

where z and t stand for the spatial coordinate and the time, respectively. The time-independent steady-state oxidation rate can therefore be predicted in this way. This method shows potential advantages for high-throughput alloy design efforts.[45]

Apart from the numerical aspect of solving the diffusion equation for oxide phases, the thermodynamic/mobility descriptions for oxide phases need further improvements. The complete description of defect formation energy (such as for vacancies, charged species, and defect clusters) can nowadays be predicted by electronic/atomistic structure calculations,[46–49] compensating direct experimental measurements. One can see advantages and opportunities to describe the 'defect phase'[50–52] by using the CEF.

One more critical factor in treating the mass transport within the scale is the role played by the short-circuit diffusion paths, such as grain boundary (GB) diffusion, which is much faster than in the lattice. Though several phenomenological approaches are available to account for GB diffusion,[53] the sensitivity of predicted oxide thickness to the assumed GB diffusion activation energy reduction factor is rather significant (see Fig. 6).

Therefore, it would be more natural to treat GBs in oxide scales in 2/3D because of the oxide grain growth, the oxide GB structure (such as GB misorientation) dependent diffusional kinetics along oxide GBs, the space charge effect,[54,55] and possible complexities due to GB dislocations.[56] Besides, the morphology of internal oxide precipitates within the alloy substrate strongly influences the kinetics of transition to the protective scale being predicted.[57,58] Phase field (PF) models, such as the WBM (Wheeler, Boettinger and McFadden) model[59,60] as implemented in YAPFI[61] or the KKS (Kim-Kim-Suzuki) model[62] as implemented in,[63] coupled with thermodynamic and mobility models outlined in section 2.3, provide potential flexibilities for quantitative predictions of scale thickening kinetics for high-temperature oxidation/corrosion applications.

3.2 On the Carbon Transport Through Oxide Scales

Currently, there is no consensus on the transport mechanism of carbon across the oxide scale during the parabolic/cubic oxidation kinetics region. For the CO_2 oxidation of 9Cr steels, one alternative mechanism proposed for oxygen and carbon transport in the spinel—which contradicts the Wagner theory and the oxidation model described in Sects. 2.3 and 3.1—is the so-called 'available space model'[64] which involves gaseous transport through the 'nanochannels' within the scale. The rate-determining process of

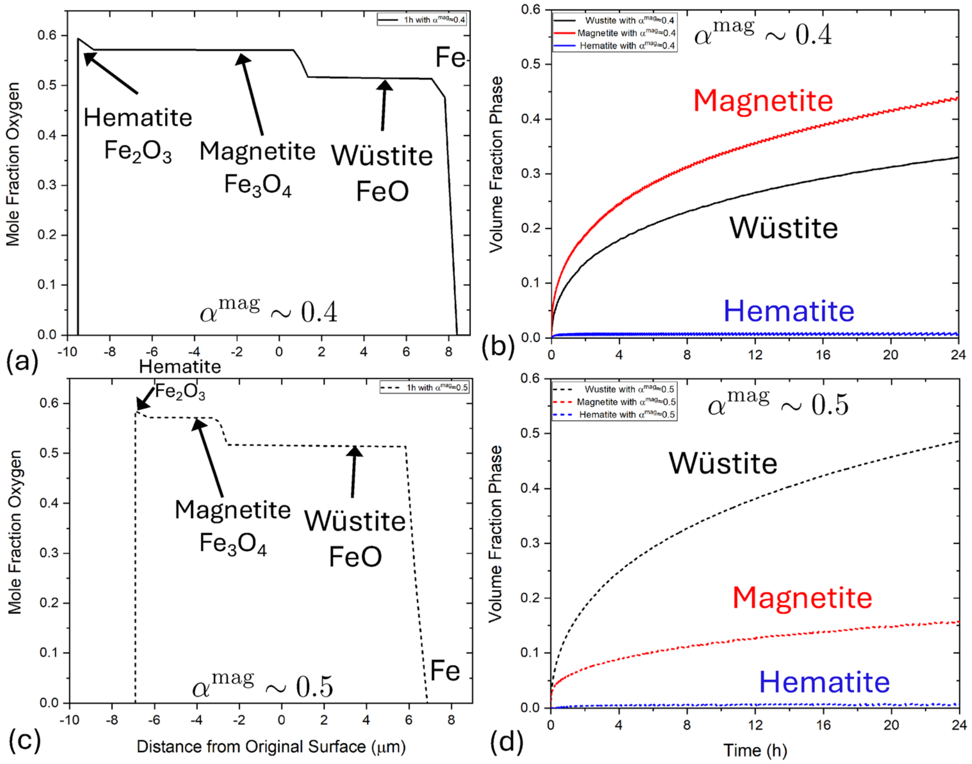

Fig. 6 Predicted oxygen concentration profiles at one hour ((a) and (c)) and evolution of oxide thickness ((b) and (d)) for Fe exposed to dry air by the homogenisation model [34]; the GB diffusion activation energy reduction factor for magnetite α^{mag} (see definition in [34]) is assumed to be 0.4 ((a) and (b)) or 0.5 ((c) and (d)). *Reproduced by permission of Wiley*

inward growth of the spinel phase is, therefore, vacancy condensation and pore formation at the scale/alloy interface, which are each determined by the outward diffusion of Fe leaving the scale/alloy interface rather than by the inward diffusion of oxygen. One advantage of this model is that it explains the observed duplex oxide structure (i.e. the equal thickness of magnetite and Cr-rich Fe spinel layers). However, there is no direct experimental observation of inter-connected ‘nanochannels’ across the scale to support the ‘available space model’. Instead, by using the atom probe tomography (APT), Young *et al.*[65] identified carbon segregation along the GB of the Cr_2O_3 scale for the Fe–20 wt.% Cr alloy exposed to an Ar–20 vol.%CO_2 environment at 650 °C, suggesting oxide GBs as plausible pathways for carbon transport within the Cr_2O_3 scale.

Therefore, a combination of solid-state diffusion along the spinel GB and gaseous transport via pores within the spinel has been proposed by Gong *et al.*.[5] Nevertheless, the lack of direct imaging of carbon within the spinel phase motivates measurements by nanoscale secondary ion mass spectrometer (Nano-SIMS), which in principle gives higher confidence in terms of chemical resolution particularly for carbon, as shown in Fig. 7 (reproduced from[11]). In this study, a P91 steel sample is exposed to a high-pressure CO_2 gaseous environment for about twenty thousand hours (for more details of alloy composition and exposure conditions, the reader is referred to[5]). The distributions of $^{56}Fe^{16}O^-$ (yellow), $^{52}Cr^{16}O^-$ (purple), $^{28}Si^-$ (red) and $^{12}C_2^-$ (green) are highlighted in Fig. 7. One can clearly see a prevalence of solid-state carbon present close to the spinel/metal interface; this justifies the modelling approach described in section 2.4 where the carbon deposited within the spinel phase increases with time while the spinel phase grows inwards. At a later exposure stage, when both the alloy substrate and the spinel phase region are saturated with carbon, breakaway occurs.[12,16] This is a plausible explanation for the breakaway effect.

Even though Eq 13 helps to rationalise the observed carbon distribution (at a large length scale) and is thus useful for lifetime assessment, it must be emphasised that the spinel phase region shows a rather complex microstructure. Figure 7 reveals two layers with distinguished features in the spinel phase region: close to the magnetite, the dense Cr-rich spinel matrix is decorated by small core/shell structure (representing oxidation of Cr-rich carbide which was also observed at the internal oxidation zone[5]), with Si enrichment and chromite phase found at spinel grain boundaries; the inner spinel phase region, however, shows larger core/shell structure, less Cr content in the matrix, more carbon-enriched phase embedded, and higher porosities. One can see more details of the above features of phases by a typical line profile taken from the inner spinel phase region, as shown in Fig. 7(d). Further detailed characterisations, such as APT analysis, are needed to locate carbon at the nanoscale.

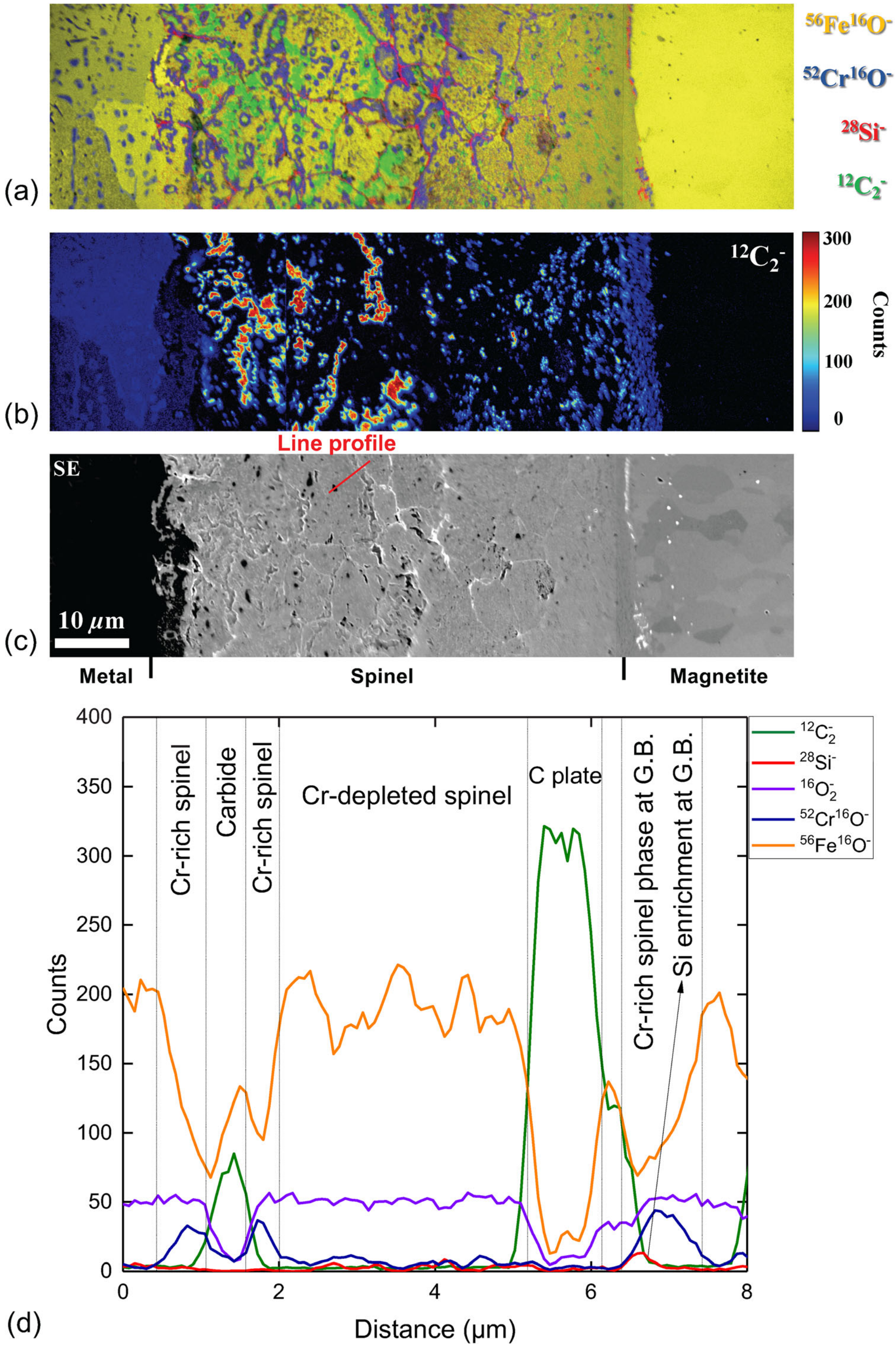

Fig. 7 Chemical mapping of oxide phase regions by NanoSIMS: (a) count distribution of $^{56}Fe^{16}O^-$ (yellow), $^{52}Cr^{16}O^-$ (purple), $^{28}Si^-$ (red) and $^{12}C_2^-$ (green); (b) count distribution of $^{12}C_2^-$; (c) secondary electron (SE) imaging; (d) selected line profile of counts (red line marked in (c)) highlighting Cr-rich spinel, carbide, Cr-depleted spinel, carbon plate and Cr-rich spinel phase and Si enrichment at grain boundaries. The figure is adapted from [11] (Color figure online)

3.3 On the Analytical Solutions for Carbon Diffusion in the Substrate

Numerical approaches make the models and associated partial differential equations (PDEs) outlined in previous sections rather easily solvable. However, the possibility of analytical solutions, often offering higher precision and efficiency, is emphasised in this section. Consider the following PDE in a 1D domain with a finite size of *L* defined within [0, *L*] where *L* is a constant,

$$\dot{C}_{\mathrm{C}}\{x,t\} = \nabla \cdot (D_{\mathrm{C}} \nabla C_{\mathrm{C}}), \qquad \text{(Eq 15)}$$

with the initial condition

$$C_C\{t=0\} = C_C^{\circ}, \tag{Eq 16}$$

and the boundary conditions

$$\begin{aligned} \alpha\left(C_C^{eq} - C_C\right) &= -D_C \frac{\partial C_C}{\partial z_x} \text{ on } x = 0 \\ \alpha\left(C_C^{eq} - C_C\right) &= +D_C \frac{\partial C_C}{\partial z_x} \text{ on } x = L \end{aligned} \tag{Eq 17}$$

where both C_C° and C_C^{eq} are materials-specific constants. The Robin boundary condition (Eq 17) resembles the interface reaction boundary conditions as described in section 2.1. Here, we outline ways to approach several cases:

- Both D_C and α are constants. The above equations can be solved by using the Sturm–Liouville theory (i.e. to use the separation of variables).[66]
- D_C is a function of C_C. In this case, we could solve it by changing the variable. For example, by defining

  $$t_1 = D_{av} t \tag{Eq 18}$$

  $$\Phi = \int_{C_C^{\circ}}^{C} \frac{D_C\{C_C\}}{D_{av}} dC \tag{Eq 19}$$

  where D_{av} is the average D_C over C_C, Eq 15 is transformed to

  $$\nabla^2 \Phi = \left[\frac{D_{av}}{D_C\{C_C\}}\right] \frac{\partial \Phi}{\partial t_1} \tag{Eq 20}$$

  By moving the non-linear part out of the Laplacian (∇^2), the transformed equation is easier to solve.[67]
- Both D_C and α are a function of t. In this case, we could first transform the time by defining

  $$t_1 = \int_0^t D_C\{t\}\, dt \tag{Eq 21}$$

Then we could use a perturbation method to solve the integral equation.[67]

Furthermore, analytical solutions show advantages in describing moving interface problems. As shown in[10] (appendix: derivation of analytical solution for oxidation), the velocity of the interface (which is controlled by the diffusion field with a constant diffusion coefficient) can be derived exactly by using a modified similarity method.

It has to be emphasised that it is challenging to use analytical solutions describing the full dependencies of PDEs simultaneously, especially for non-linear cases. However, analytical solutions offer a baseline to test numerical implementations for several fairly complex ideal situations.

3.4 On the Prediction of Breakaway Oxidation by Kinetic Modelling

Once the component with a finite size is saturated with carbon by the Boudouard reaction, excess carbon will be deposited on the metal/oxide interface and within the spinel phase region. The consequent volume expansion damages the scale, destroying its semi-protective character. Besides, because the steel is by then carburised, insufficient chromium remains in the ferrite to heal the scale, leading to breakaway initiations. Such phenomena motivate the life-assessment strategy based on the carbon saturation in the substrate of the component.[10] We first correlate the measured carbon uptake kinetics and the breakaway initiation kinetics by assuming a critical value of carbon uptake defining the saturation. We can then confidently extrapolate the carbon uptake kinetics from high to low-temperature regions based on physical models described in section 2. The breakaway initiation at low temperatures, which has never happened, can therefore be predicted based on low-temperature carbon uptake kinetics and the critical carbon uptake assumed. As shown in Fig. 8, the predicted time to carbon saturation (TCS) is strongly correlated with the time to breakaway initiation (ttb). By reducing the exposure temperature, the lifetime of the component can be significantly extended.

4 Summary and Conclusions

Computational modelling of phase transformations in metals and alloys is evolving to greater and greater complexity, driven by (i) more sophisticated kinetic treatments for diffusion-assisted transformation, (ii) ever-improving thermodynamic and kinetics databases and (iii) the wider availability of low-cost computing hardware. This situation is allowing more and more sophisticated calculations to be carried out of significant engineering relevance—for example, the true alloy compositional complexity can be handled together with reactions from gaseous media. In this article, we have demonstrated this to be the case, by focussing on recent progress concerning the degradation of 9Cr steels in high-temperature CO_2. Numerical models describing the oxidation kinetics, the non-steady-state carburisation kinetics, and the coupling between them have been introduced. The current challenges and future developments of the defect-chemistry-based oxidation model have been highlighted. The mechanism of carbon transport has been discussed concerning the complex microstructure revealed in the spinel phase region. The derivation of analytical solutions for solving the carbon concentration field is briefly summarised. Furthermore, the carbon uptake models described in this paper can well rationalise

Fig. 8 Predicted time to carbon saturation (TCS) and measured time to breakaway initiation (ttb) [10]

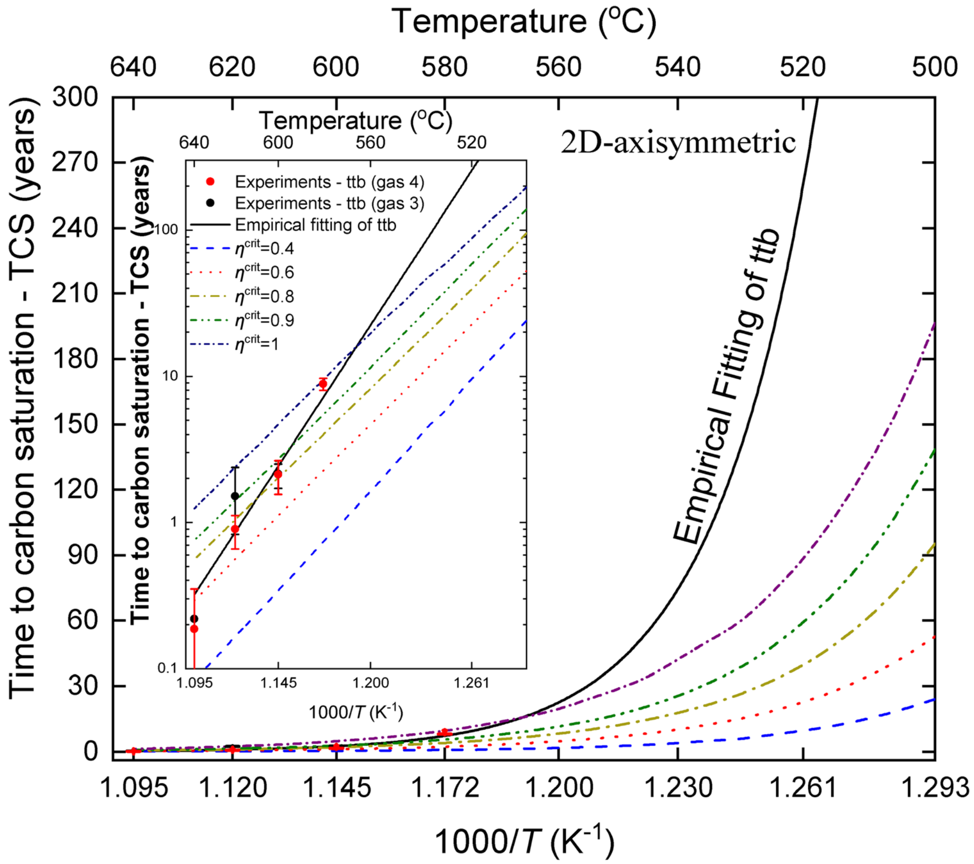

measured carbon uptake kinetics across a wide range of temperatures for components with complex geometries; this makes the lifetime prediction, which is based on carbon saturation kinetics, possible.

Acknowledgments The authors thank EDF Energy for funding this work over many years. They are particularly grateful to Dr Aya Shin and Dr Jonathan Pearson for their support. Dr. Kexue Li is acknowledged for performing the Nano-SIMS measurements. Fruitful discussions with Prof. David J. Young, Dr. Bruce Pint, Dr. Reza Naraghi, Prof. Jörg Neugebauer, and Prof. Dierk Raabe are sincerely acknowledged.

References

1. M. Hillert, *Phase Equilibria, Phase Diagrams and Phase Transformations: Their Thermodynamic Basis*. Cambridge University Press, Cambridge, 2007. https://doi.org/10.1017/CBO9780511812781
2. M. Hillert, Diffusion and Interface Control of Reactions in Alloys, *Metall. Trans. A*, 1975, **6**(1), p 5–19.
3. R. Allam, S. Martin, B. Forrest, J. Fetvedt, X.J. Lu, D. Freed, G.W. Brown, T. Sasaki, M. Itoh, J. Manning, Demonstration of the Allam Cycle: An update on the development status of a high efficiency supercritical carbon dioxide power process employing full carbon capture, 13th international conference on greenhouse gas control technologies*, Ghgt-13*, **114**, 5948-5966 (2017) (in English)
4. X.R. Zhang, H. Yamaguchi, D. Uneno, K. Fujima, M. Enomoto, and N. Sawada, Analysis of a Novel Solar Energy-Powered Rankine Cycle for Combined Power and Heat Generation Using Supercritical Carbon Dioxide, *Renew. Energy*, 2006, **31**(12), p 1839–1854.
5. Y. Gong, D.J. Young, P. Kontis, Y.L. Chiu, H. Larsson, A. Shin, J.M. Pearson, M.P. Moody, and R.C. Reed, On the Breakaway Oxidation of Fe9Cr1Mo Steel in High Pressure CO2$_2$, *Acta Mater.*, 2017, **130**, p 361–374.
6. B.A. Pint, R.G. Brese, and J.R. Keiser, Effect of Pressure on Supercritical CO_2 Compatibility of Structural Alloys at 750 °C, *Mater. Corros.*, 2017, **68**(2), p 151–158.
7. J.R. DiStefano, V.K. Sikka, J.J. Blass, C.R. Brinkman, J.M. Corum, J.A. Horak, R.L. Huddleston, J.F. King, R.W. McClung, W.K. Sartory, Summary of modified 9Cr-1Mo steel development program, 1975-1985, 1986

8. D.J. Young, High Temperature Oxidation and Corrosion of Metals, Second ed., Elsevier, 2016
9. J.L. Meijering, Internal Oxidation in Alloys, 3rd ed., Wiley-Interscience, 1971
10. Y.L. Gong, S.P.A. Gill, S.B.A. Yan, R. Higginson, J. Sumner, N.J. Simms, H. Larsson, A. Shin, J.M. Pearson, D.J. Young, C. Atkinson, A.C.F. Cocks, and R.C. Reed, Assessment of Corrosive Attack of Fe9Cr1Mo Alloys in Pressurised CO2 for Prediction of Breakaway Oxidation, *Corros. Sci.*, 2023, **222**, 111385.
11. Y. Gong, "Modelling of Diffusional Phenomena in Structural Alloys for High Temperature Applications," University of Oxford, 2017
12. Y. Gong, D.J. Young, C. Atkinson, T. Olszewski, W.J. Quadakkers, and R.C. Reed, Modelling of the Degradation of Martensitic Stainless Steels by the Boudouard Reaction, *Corros. Sci.*, 2020, **173**, 108699. **(in English)**
13. D.J. Young, and J. Zhang, Corrosion by Hot CO_2 Gases, *Electrochem. Soc. Interface*, 2021, **30**(2), p 73–77.
14. L. Coghlan, S. Yan, A. Shin, J. Pearson, M.A.E. Jepson, and R.L. Higginson, The effect of Microstructure on the Oxidation and Carburisation of 9Cr-1Mo Steel Exposed to CO, *Corros. Sci.*, 2021, **191**, 109720. **(in English)**
15. K.E. Nygren, Z. Yu, F. Rouillard, and A. Couet, Effect of Sample Thickness on the Oxidation and Carburization Kinetics of 9Cr-1Mo Steel in High and Atmospheric Pressure CO_2 at 550 °C, *Corros. Sci.*, 2020, **163**, 108292.
16. M.S.A. Karunaratne, S. Yan, R.C. Thomson, L. Coghlan, and R.L. Higginson, Modelling Carburisation in 9Cr-1Mo Ferritic Steel Tube Substrates in Experimental CO_2 Atmospheres, *Corros. Sci.*, 2020, **163**, 108248.
17. M. Hillert, B. Jansson, and B. Sundman, Application of the Compound-Energy Model to Oxide Systems/ Anwendung des "Compound-Energy"-Modells auf Oxidsysteme, *Int. J. Mater. Res.*, 1988, **79**(2), p 81–87.
18. M. Hillert, The Compound Energy Formalism, *J. Alloy. Compd.*, 2001, **320**(2), p 161–176.
19. M. Hillert, The Discrete Lattice Model for Diffusion Revisited, *Scripta Mater.*, 2001, **44**(7), p 1095–1097.
20. F. Rouillard, G. Moine, M. Tabarant, and J.C. Ruiz, Corrosion of 9Cr Steel in CO2 at Intermediate Temperature II: Mechanism of Carburization, *Oxid. Met.*, 2012, **77**(1–2), p 57–70.
21. D. Young, P. Huczkowski, T. Olszewski, T. Hüttel, L. Singheiser, and W.J. Quadakkers, Non-Steady State Carburisation of Martensitic 9–12% Cr Steels in CO_2 Rich Gases at 550 °C, *Corros. Sci.*, 2014, **88**, p 161–169.
22. T. Gheno, D. Monceau, J. Zhang, and D.J. Young, Carburisation of Ferritic Fe–Cr Alloys by Low Carbon Activity Gases, *Corros. Sci.*, 2011, **53**(9), p 2767–2777.
23. H. Yin, J. Zhang, and D.J. Young, Effect of Gas Composition on Coking and Metal Dusting of 2.25Cr–1Mo Steel Compared with Iron, *Corr. Sci.*, 2009, **51**(12), p 2983–2993.
24. H. Eyring, The Activated Complex in Chemical Reactions, *J. Chem. Phys.*, 1935, **3**(2), p 107–115.
25. H. Larsson, and L. Höglund, Multiphase Diffusion Simulations in 1D Using the DICTRA Homogenization Model, *Calphad*, 2009, **33**(3), p 495–501. https://doi.org/10.1016/j.calphad.2009.06.004
26. H. Larsson, and A. Engström, A Homogenization Approach to Diffusion Simulations Applied to $\alpha+\gamma$ Fe–Cr–Ni Diffusion Couples, *Acta Mater.*, 2006, **54**(9), p 2431–2439.
27. O. Wiener, Der abhandlungen der mathematisch-physischen klasse der Konigl, *Sachsischen Gesellshaft der Wissenschaften*, 1912, **32**, p 509–604.
28. R. Jones, D.W. Beardsmore, TUBELIFE 6.0 Specification, 2014
29. J.O. Andersson, and J. Ågren, Models for Numerical Treatment of Multicomponent Diffusion in Simple Phases, *J. Appl. Phys.*, 1992, **72**(4), p 1350–1355.
30. J.S. Kirkaldy, D.J. Young, Diffusion in the condensed state, Institute of Metals ; Institute of Metals North American Publications Center [distributor for] North America London, Brookfield, VT, USA, 1987, p xiv, 527 pages : illustrations ; 25 cm
31. H.K.D.H. Bhadeshia, Diffusional Formation of Ferrite in Iron and its Alloys, *Prog. Mater. Sci.*, 1985, **29**(4), p 321–386.
32. A. Atkinson, Transport Processes During the Growth of Oxide Films at Elevated Temperature, *Rev. Mod. Phys.*, 1985, **57**(2), p 437–470.
33. C. Wagner, Equations for Transport in Solid Oxides and Sulfides of Transition Metals, *Prog. Solid State Chem.*, 1975, **10**, p 3–16.
34. H. Larsson, T. Jonsson, R. Naraghi, Y. Gong, R.C. Reed, and J. Ågren, Oxidation of Iron at 600 °C—Experiments and Simulations, *Mater. Corros.*, 2016, **68**(2), p 133–142.
35. K. Akiba, M. Ueda, K. Kawamura, and T. Maruyama, Quantitative Prediction of Voids Formation in a Growing Nickel Oxide Scale at 1373 K, *Mater. Trans.*, 2007, **48**(10), p 2753–2761.
36. B. Sundman, An Assessment of the Fe-O System, *Journal of Phase Equilibria*, 1991, **12**(2), p 127–140.
37. Y. Gong, Synergy between Experimentation and Modelling for Life-time Prediction and Design against Corrosion, Gordon Research Conference in High Temperature Corrosion: Degradation Mechanisms, Life Prediction and Improved Materials for Application in Extreme Environments, B. Pint Ed., 2023
38. R. Naraghi, L. Höglund, and J. Ågren, [O33] Application of Compound-Energy Formalism to the Parabolic Growth of Solid Metal Oxides, *Calphad*, 2015, **51**, p 355.
39. S. Hallström, L. Höglund, and J. Ågren, Modeling of Iron Diffusion in the Iron Oxides Magnetite and Hematite with Variable Stoichiometry, *Acta Mater.*, 2011, **59**(1), p 53–60.
40. S. Hallström, "On high temperature oxidation resistance : Towards the materials genome of high temperature alloys," Doctoral thesis, comprehensive summary, KTH Royal Institute of Technology, 2014
41. R. Naraghi, manuscript in preparation,
42. S. Bigdeli, L. Kjellqvist, R. Naraghi, L. Höglund, H. Larsson, and T. Jonsson, Strategies for High-Temperature Corrosion Simulations of Fe-Based Alloys Using the Calphad Approach: Part I, *J. Phase Equilib. Diffus.*, 2021, **42**(3), p 403–418.
43. H. Larsson, and L. Höglund, A Scheme for More Efficient Usage of CALPHAD Data in Simulations, *Calphad*, 2015, **50**, p 1–5.
44. H. Larsson, On the Use of Boltzmann's Transformation to Solve Diffusion Problems, *Calphad*, 2021, **73**, 102261.
45. A. Sato, Y.L. Chiu, and R.C. Reed, Oxidation of Nickel-Based Single-Crystal Superalloys for Industrial Gas Turbine Applications, *Acta Mater.*, 2011, **59**(1), p 225–240.
46. C. Freysoldt, B. Grabowski, T. Hickel, J. Neugebauer, G. Kresse, A. Janotti, and C.G. Van de Walle, First-Principles Calculations for Point Defects in Solids, *Rev. Mod. Phys.*, 2014, **86**(1), p 253–305.
47. A. Glensk, B. Grabowski, T. Hickel, and J. Neugebauer, Understanding Anharmonicity in fcc Materials: From its Origin to ab Initio Strategies Beyond the Quasiharmonic Approximation, *Phys. Rev. Lett.*, 2015, **114**(19), 195901.
48. Y. Gong, B. Grabowski, A. Glensk, F. Körmann, J. Neugebauer, and R.C. Reed, Temperature Dependence of the Gibbs Energy of Vacancy Formation of fcc Ni, *Phys. Rev. B*, 2018, **97**(21), 214106.
49. A.P. Chen, W.M.C. Foulkes, A.H. Heuer, and M.W. Finnis, Diffusion of Oxygen in Mg-doped α-Al_2O_3: The Corundum Conundrum Explained, *Phys. Rev. Mater.*, 2022, **6**(6), 063404.
50. S. Korte-Kerzel, T. Hickel, L. Huber, D. Raabe, S. Sandlöbes-Haut, M. Todorova, and J. Neugebauer, Defect Phases—Thermodynamics and Impact on Material Properties, *Int. Mater. Rev.*, 2022, **67**(1), p 89–117.

51. R. Kirchheim, Reducing Grain Boundary, Dislocation Line and Vacancy Formation Energies by Solute Segregation. I. Theoretical Background, *Acta Mater.*, 2007, **55**(15), p 5129–5138. https://doi.org/10.1016/j.actamat.2007.05.047
52. R. Kirchheim, Revisiting Hydrogen Embrittlement Models and Hydrogen-Induced Homogeneous Nucleation of Dislocations, *Scripta Mater.*, 2010, **62**(2), p 67–70.
53. I. Kaur, W. Gust, Fundamentals of grain and interphase boundary diffusion, 2nd rev. ed., Ziegler Press, 1989
54. M.P. Tautschnig, N.M. Harrison, and M.W. Finnis, A Model for Time-Dependent Grain Boundary Diffusion of Ions and Electrons Through a Film or Scale, with an Application to Alumina, *Acta Mater.*, 2017, **132**, p 503–516.
55. K. Kim, Q.C. Sherman, L.K. Aagesen, and P.W. Voorhees, Phase-Field Model of Oxidation: Kinetics, *Phys. Rev. E*, 2020, **101**(2), 022802.
56. A.H. Heuer, Oxygen and Aluminum Diffusion in α-Al_2O_3: How Much do We Really Understand?, *J. Eur. Ceram. Soc.*, 2008, **28**(7), p 1495–1507.
57. R. Wang, Y. Ji, T.-L. Cheng, F. Xue, L.-Q. Chen, and Y.-H. Wen, Phase-Field Modeling of Alloy Oxidation at High Temperatures, *Acta Mater.*, 2023, **248**, 118776.
58. W. Zhao, Y. Kang, J.M.A. Orozco, and B. Gleeson, Quantitative Approach for Determining the Critical Volume Fraction for the Transition from Internal to External Oxidation, *Oxid. Met.*, 2015, **83**(3), p 187–201.
59. A.A. Wheeler, W.J. Boettinger, and G.B. McFadden, Phase-Field Model for Isothermal Phase Transitions in Binary Alloys, *Phys. Rev. A*, 1992, **45**(10), p 7424–7439.
60. A.A. Wheeler, W.J. Boettinger, and G.B. McFadden, Phase-Field Model of Solute Trapping During Solidification, *Phys. Rev. E*, 1993, **47**(3), p 1893–1909.
61. H. Larsson, The YAPFI Phase-Field Implementation, *arXiv preprint* arXiv:2104.11501, (2021)
62. S.G. Kim, W.T. Kim, and T. Suzuki, Phase-Field Model for Binary Alloys, *Phys. Rev. E*, 1999, **60**(6), p 7186–7197.
63. D. Schwen, L.K. Aagesen, J.W. Peterson, and M.R. Tonks, Rapid Multiphase-Field Model Development Using a Modular Free Energy Based Approach with Automatic Differentiation in MOOSE/MARMOT, *Comput. Mater. Sci.*, 2017, **132**, p 36–45.
64. F. Rouillard, G. Moine, L. Martinelli, and J.C. Ruiz, Corrosion of 9Cr Steel in CO_2 at Intermediate Temperature I: Mechanism of Void-Induced Duplex Oxide Formation, *Oxid. Met.*, 2012, **77**(1), p 27–55.
65. D.J. Young, T.D. Nguyen, P. Felfer, J. Zhang, and J.M. Cairney, Penetration of Protective Chromia Scales by Carbon, *Scripta Mater.*, 2014, **77**, p 29–32.
66. W.O. Amrein, A.M. Hinz, D.B. Pearson, Sturm-Liouville Theory: Past and Present, Springer Science & Business Media, 2005
67. Y. Gong, C. Atkinson, manuscript in preparation,